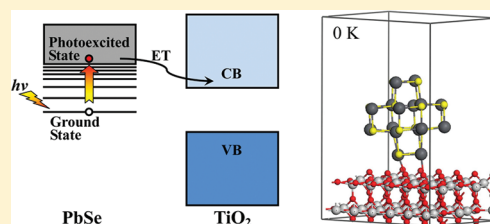


Ab Initio Nonadiabatic Molecular Dynamics of the Ultrafast Electron Injection from a PbSe Quantum Dot into the TiO<sub>2</sub> SurfaceRun Long<sup>†,‡</sup> and Oleg V. Prezhdo<sup>\*,†</sup><sup>†</sup>Department of Chemistry, University of Rochester, New York 14627, United States<sup>‡</sup>School of Chemical & Bioprocess Engineering, University College Dublin, Ireland

S Supporting Information

**ABSTRACT:** Following recent experiments [*Science* **2010**, 328, 1543; *PNAS* **2011**, 108, 965], we report an *ab initio* nonadiabatic molecular dynamics (NAMD) simulation of the ultrafast photoinduced electron transfer (ET) from a PbSe quantum dot (QD) into the rutile TiO<sub>2</sub> (110) surface. The system forms the basis for QD-sensitized semiconductor solar cells and demonstrates that ultrafast interfacial ET is instrumental for achieving high efficiencies in solar-to-electrical energy conversion. The simulation supports the observation that the ET successfully competes with energy losses due to electron–phonon relaxation. The ET proceeds by the adiabatic mechanism because of strong donor–acceptor coupling. High frequency polar vibrations of both QD and TiO<sub>2</sub> promote the ET, since these modes can rapidly influence the donor–acceptor state energies and coupling. Low frequency vibrations generate a distribution of initial conditions for ET, which shows a broad variety of scenarios at the single-molecule level. Compared to the molecule–TiO<sub>2</sub> interfaces, the QD–TiO<sub>2</sub> system exhibits pronounced differences that arise due to the larger size and higher rigidity of QDs relative to molecules. Both donor and acceptor states are more delocalized in the QD system, and the ET is promoted by optical phonons, which have relatively low frequencies in the QD materials composed of heavy elements. In contrast, in molecular systems, optical phonons are not thermally accessible under ambient conditions. Meanwhile, TiO<sub>2</sub> acceptor states resemble surface impurities due to the local influence of molecular chromophores. At the same time, the photoinduced ET at both QD–TiO<sub>2</sub> and molecule–TiO<sub>2</sub> interfaces is ultrafast and occurs by the adiabatic mechanism, as a result of strong donor–acceptor coupling. The reported state-of-the-art simulation generates a detailed time-domain atomistic description of the interfacial ET process that is fundamental to a wide variety of applications.



## 1. INTRODUCTION

Interfacial electron transfer (ET, Figure 1) plays a key role in many areas of research, and numerous efforts have been devoted to exploring its nature and mechanisms. Various aspects of interfacial ET<sup>1</sup> draw close scrutiny in molecular electronics,<sup>2,3</sup> photovoltaics,<sup>4–8</sup> solar hydrogen production,<sup>9,10</sup> electrolysis,<sup>11</sup> catalysis,<sup>12,13</sup> photochemistry,<sup>14,15</sup> and photosynthesis.<sup>16</sup> These and other applications involve a great variety of interfaces, composed of both organic and inorganic species with zero-, one-, two-, and three-dimensional properties. Solar energy harvesting alone encounters interfaces between covalently<sup>17</sup> and non-covalently<sup>18,19</sup> bound molecular species, two inorganic materials,<sup>20,21</sup> inorganic and organic semiconductors,<sup>22</sup> polymers,<sup>23,24</sup> all-carbon structures of different dimensionalities,<sup>25</sup> molecular and bulk moieties,<sup>26</sup> quasi-zero-dimensional and three-dimensional inorganic semiconductors of different types,<sup>27,28</sup> etc. The properties of individual species forming these systems are understood much better than the interactions at the surface. The challenge resides in the often contrasting characteristics of the two interface components, e.g. localized vs delocalized electronic states, high vs low frequency phonon modes, soft organic vs hard inorganic materials, good vs poor conductors of electricity and heat, well-ordered vs disordered phases, and so on. Additional complications arise because the

disparate sets of theories used to describe these materials have been developed within different disciplines, including chemistry, physics, biology, and engineering.<sup>8</sup>

Dye-sensitized semiconductor solar cells (DSSCs) constitute a promising alternative to the traditional silicon based cells, due to a combination of low cost and good efficiency. Stimulated by the original work of O'Regan and Graetzel,<sup>29</sup> and many experiments to follow,<sup>4,5,30</sup> dozens of theoretical studies have been reported on DSSCs in the past ten years, focusing on chromophore–semiconductor binding,<sup>31–33</sup> electronic structure,<sup>34–37</sup> and direct simulation of the electron injection.<sup>38–43</sup>

Our group has initiated the time-domain *ab initio* modeling of the interfacial electron dynamics, including both electronic donor–acceptor and electron–phonon interactions.<sup>7,44–49</sup> We have been able to describe the whole spectrum of processes occurring at the chromophore–semiconductor interface, starting from chromophore photoexcitation, resulting in charge separation, delocalization, and relaxation, accompanied by electron trapping at the surface and its transfer back to the chromophore or electrolyte, and concluding with regeneration of neutral

Received: September 12, 2011

Published: October 18, 2011

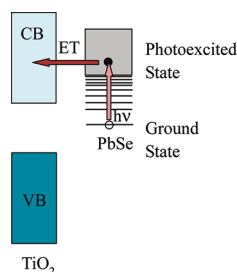


**Figure 1.** Schematic of the photoinduced electron injection process. Photon absorption promotes an electron from the ground state of the PbSe quantum dot located inside the  $\text{TiO}_2$  band gap into an excited state that is in resonance with the conduction band (CB). Then, the excited electron is injected into the  $\text{TiO}_2$  CB.

chromophore by ET from electrolyte. Using the same state-of-the-art technique, we have investigated<sup>50</sup> the closely related photoinduced ET at the semiconductor–water interface.<sup>51</sup>

More recently, the solar cell community has begun to explore photovoltaic designs employing quantum dot (QD) chromophores for semiconductor sensitization.<sup>27,28,52–55</sup> Compared to molecular chromophores, which can be photochemically unstable and harvest only part of the solar spectrum, QDs are easily tunable to absorb light at any wavelength, have high extinction coefficients and large intrinsic dipole moments, and are photochemically robust. In addition, QDs provide opportunities for increasing a solar cell's voltage and current, by either extracting hot charge carriers or using the additional energy available at the blue end of the solar spectrum for generating multiple electron–hole pairs.<sup>27</sup> The interplay between the electron–phonon relaxation and multiple exciton generation (MEG) has drawn an enormous amount of attention.<sup>54,56–70</sup> Driven by the MEG prospect to increase the thermodynamic efficiency of an ideal single-cell photovoltaic device from the 32% Shockley–Queisser<sup>71</sup> detailed balance limit to 44%,<sup>60</sup> a potentially huge photovoltaic advance, a number of contradicting observations have been reported in the literature regarding the rates of electron–phonon relaxation and the mechanisms and efficiencies of MEG. Complementary to other experimental<sup>56–64</sup> and theoretical<sup>57,65–70</sup> efforts, our *ab initio* modeling,<sup>54,72–79</sup> including time-domain simulations,<sup>53,80–85</sup> has helped to resolve many of these controversies. In particular, we have established that the electron–phonon relaxation is fast at the energies relevant to MEG and that the so-called phonon bottleneck can be observed only at low energies near the QD band gap.<sup>80,81</sup> Ligands on the QD surface<sup>70</sup> can greatly accelerate the energy losses.<sup>82</sup> We have argued that direct photogeneration of multiply excited electronic states can explain MEG in the presence of rapid electron–phonon relaxation.<sup>75</sup> We have shown that QD defects, such as charges, dopants, and dangling bonds, greatly diminish MEG efficiencies.<sup>74,76</sup> Our latest, most advanced time-domain study of Auger processes including nearly 100,000 excited electronic states has demonstrated that MEG can be assisted by phonons and that exciton annihilation is preceded by electronic energy relaxation.<sup>83</sup>

The current theoretical study on the photoinitiated ET from a PbSe QD into the  $\text{TiO}_2$  surface is stimulated by the recent experiments in the laboratories of Zhu<sup>86,87</sup> and Parkinson.<sup>28</sup> Zhu and co-workers<sup>86,87</sup> employed a pump–probe laser technique to report an ultrafast extraction of hot electrons from excited PbSe QDs into the  $\text{TiO}_2$  semiconductor. They showed that scattering of photoexcited electrons in the QD conduction band (CB) occurs faster than electron cooling, resulting in a quasi-equilibrium where

the electronic temperature is much higher than the lattice temperature. As a result, hot electrons can be extracted faster than they lose energy to phonons, thereby potentially increasing the solar cell voltage. A few months later, Parkinson and co-workers<sup>28</sup> demonstrated that MEG in PbS QDs adsorbed on  $\text{TiO}_2$  can be used to increase solar cell currents by producing photon-to-current yields higher than 100%. These experimental findings provide strong motivation for development of QD solar cells (QDSCs). The extremely fast, sub-50-fs ET from the PbSe QDs into the  $\text{TiO}_2$  surface<sup>86,87</sup> makes it difficult to invoke traditional ET models, such as the Marcus theory, which requires slow ET dynamics to allow for redistribution of vibrational energy. A time-domain simulation of the injection process becomes necessary. As demonstrated with the DSSC<sup>7,44–49</sup> and QD<sup>46,72–77</sup> studies, an atomistic description complements phenomenological models and provides many valuable and often critical insights into the photoinduced electron dynamics.

The present work combines nonadiabatic molecular dynamics (NAMD) with time-domain density functional theory (TDDFT),<sup>49,88–90</sup> to investigate the photoexcited ET process at the QD– $\text{TiO}_2$  interface. The simulation shows that the interfacial ET in QDSC exhibits both similarities and differences compared to DSSC. The differences arise because QDs are significantly larger, more rigid, and composed of heavier elements than molecules. The similarities rely on strong electron donor–acceptor coupling in both types of systems. Our study demonstrates that, indeed, the ultrafast QD– $\text{TiO}_2$  ET competes successfully with electron relaxation inside the QD. The ET proceeds primarily by the adiabatic mechanism, and the NA mechanism contributes little, in spite of the diversity of individual ET events. Analysis of the vibrational modes shows that polar optical phonons of both donor and acceptor species are primarily responsible for the ET process across the QD– $\text{TiO}_2$  interface. This is in contrast to the DSSC systems, in which low-frequency acoustic-type modes drive the transfer. By analyzing the dimensionality of the electron donor and acceptor states, the strength of the donor–acceptor coupling, and the active vibrational modes, we discuss the similarities and differences in the photoinduced ET dynamics in the QD– $\text{TiO}_2$ , molecule– $\text{TiO}_2$ , and wet-electron systems, and we establish the fundamental mechanisms underlying the interfacial ET processes.

The paper is organized as follows. The next section summarizes the theory underlying NAMD and TDDFT, and it presents the necessary computational details. The Results and Discussion section is separated into three parts devoted to the geometric and electronic structure of the QD– $\text{TiO}_2$  interface, the vibrational motions participating in the ET dynamics, and the mechanisms responsible for the electron injection process. Continuously throughout this section, the results obtained for the QD– $\text{TiO}_2$  system are compared with our earlier calculations on the photoinduced electron injection across the  $\text{TiO}_2$ –molecule<sup>7,44–49</sup> and  $\text{TiO}_2$ –water<sup>50</sup> interfaces. The Conclusions section summarizes the key findings of the current work.

## 2. THEORETICAL METHODOLOGY

The detailed description of the theoretical approach,<sup>42,79–81</sup> combining NAMD with TDDFT, can be found in our previous publications. Among other applications,<sup>53,80–85,90–92</sup> the approach was used to study the ET and relaxation dynamics in the chromophore– $\text{TiO}_2$  and wet-electron systems.<sup>7,44–50</sup> The following subsection provides the technical details of the standard DFT and MD techniques<sup>93</sup> as they are applied to

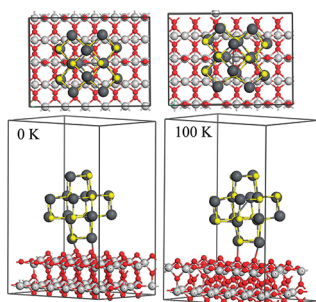


**Figure 2.** Side and surface views of the simulation cell showing the geometry of the rutile(110)–PbSe–QD system optimized at 0 K (left) and during the molecular dynamics run at 100 K (right). Thermal fluctuations influence the system geometry and, hence, its electronic structure.

the PbSe–TiO<sub>2</sub> system. Then, the fundamental theory behind our state-of-the-art TDDFT–NAMD method is briefly reviewed, and the necessary specifics of the time-domain simulation are given.

**2.1. Simulation Details.** The stoichiometric rutile (110) surface was modeled with a periodically repeated slab. A 144-atom (6 × 2) surface comprised six atomic layers of TiO<sub>2</sub>, with the bottom three layers frozen in the bulk configuration. The slab was separated from its periodic image along the surface normal by a vacuum region of 20 Å. The PbSe QD was represented by the Pb<sub>16</sub>Se<sub>16</sub> cluster, which is the smallest stable PbSe system preserving the semiconductor bulk structure during geometry optimization and finite-temperature molecular dynamics simulation.<sup>80</sup> The PbSe QD binds strongly to the TiO<sub>2</sub> surface via two Pb atoms interacting with two bridging oxygen atoms of the surface, as shown in Figure 2.

The geometry optimization, electronic structure, and adiabatic MD calculations were carried out using the Vienna ab initio simulation package (VASP).<sup>94</sup> The nonlocal exchange and correlation energies were treated with the Perdew–Burke–Ernzerhof (PBE) functional,<sup>95</sup> which is based on the generalized gradient approximation (GGA). The projector-augmented wave (PAW) approach was used to describe the interaction of the ionic cores with the valence electrons.<sup>96</sup> After relaxing the geometry at 0 K, repeated velocity rescaling was used to bring the temperature of the TiO<sub>2</sub>–PbSe system to 100 K, corresponding to the low temperature in the experiment.<sup>86</sup> After that, a 2 ps adiabatic MD simulation was performed in the microcanonical ensemble with a 1 fs atomic time step. The atomic trajectories from this adiabatic MD were used to sample the initial conditions and to carry out the NAMD simulations.

**2.2. Nonadiabatic Molecular Dynamics with Time-Domain Density Functional Theory.** The ET dynamics including the NA effects<sup>97</sup> are described by real-time TDDFT within the Kohn–Sham (KS) approach.<sup>42,79–81</sup> The electron density  $\rho(\mathbf{r},t)$  is expressed within the KS approach by a sum of the densities of the occupied single-electron KS orbitals  $\varphi_p(\mathbf{r},t)$ . The evolution of the electron density is determined by the time-dependent variational principle, leading to a set of single-particle equations for the evolution of the KS orbitals:

$$i\hbar \frac{\partial \varphi_p(\mathbf{r},t)}{\partial t} = H(\mathbf{r},\mathbf{R},t) \varphi_p(\mathbf{r},t) \quad (1)$$

where  $p = 1, 2, \dots, N_e$ , and  $N_e$  is the number of electrons. These single-electron equations are coupled, because the DFT functional  $H$  depends on the sum of the densities of all occupied KS orbitals. The Hamiltonian  $H$  is time-dependent through the external potential created by the motion of the atoms.

The single-electron orbitals in eq 1 are expressed in the basis of the adiabatic KS orbitals  $\tilde{\varphi}_p(\mathbf{r},\mathbf{R}(t))$ , which are obtained with time-independent DFT for the atomic positions in each step of the adiabatic MD

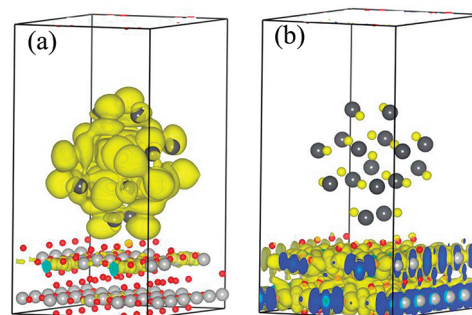


**Figure 3.** Charge densities of (a) donor and (b) acceptor states.

simulation. The focus is on the evolution of the orbital  $\varphi_{\text{PE}}$  occupied by the photoexcited electron. As discussed previously,<sup>47,98</sup> the ET dynamics are well described by the evolution of the PE electron, which involves unoccupied orbitals of the Pb<sub>16</sub>Se<sub>16</sub> cluster and TiO<sub>2</sub> CB states. All other electrons and orbitals are significantly separated in energy from the photoexcited electron. The inclusion of the other states is only necessary when the longer time dynamics associated with the electron relaxation to the ground state are of interest.<sup>44</sup>

The adiabatic basis set representation of the PE electron orbital is given in eq 2

$$\varphi_{\text{PE}}(\mathbf{r},t) = \sum_k c_k(t) \tilde{\varphi}_k(\mathbf{r};\mathbf{R}(t)) \quad (2)$$

Inserting eq 2 into eq 1 leads to the equation describing the evolution of the adiabatic states expansion coefficients:

$$i\hbar \frac{\partial}{\partial t} c_j(t) = \sum_k c_k(t) (\varepsilon_k \delta_{jk} + d_{jk}) \quad (3)$$

where  $\varepsilon_k$  is the energy of the adiabatic state  $k$ , and  $d_{jk}$  is the NA coupling between states  $k$  and  $j$ . The coupling is created by atomic motions that generate parametric dependence of the time-independent adiabatic KS orbitals on atomic coordinates and, hence, time. The NA coupling represents the interaction of the electronic degrees of freedom with phonons. It is given by

$$d_{jk} = -i\hbar \langle \tilde{\varphi}_j | \nabla_{\mathbf{R}} | \tilde{\varphi}_k \rangle \frac{d\mathbf{R}}{dt} = -i\hbar \langle \tilde{\varphi}_j | \frac{\partial}{\partial t} | \tilde{\varphi}_k \rangle \quad (4)$$

The extent of ET from the PbSe QD to the TiO<sub>2</sub> surface is evaluated by integrating the electron density over the region of the simulation cell occupied by the PbSe QD, as shown in Figures 2 and 3.

$$\begin{aligned} \int_{\text{QD}} \rho_{\text{PE}}(\mathbf{r},t) d\mathbf{r} &= \int_{\text{QD}} |\varphi_{\text{PE}}(\mathbf{r},t)|^2 d\mathbf{r} \\ &= \sum_{k,j} c_k^*(t) c_j(t) \int_{\text{QD}} \tilde{\varphi}_k^*(\mathbf{r},\mathbf{R}(t)) \tilde{\varphi}_j(\mathbf{r},\mathbf{R}(t)) d\mathbf{r} \end{aligned} \quad (5)$$

Taking the time-derivative of eq 5 gives expressions for the adiabatic and NA contributions to the ET:<sup>49</sup>

$$\frac{d \int_{\text{QD}} \rho_{\text{PE}}(\mathbf{r},t) d\mathbf{r}}{dt} = \sum_{k,j} \left\{ \frac{d(c_k^* c_j)}{dt} \int_{\text{QD}} \tilde{\varphi}_k^* \tilde{\varphi}_j d\mathbf{r} + c_k^* c_j \frac{d \int_{\text{QD}} \tilde{\varphi}_k^* \tilde{\varphi}_j d\mathbf{r}}{dt} \right\} \quad (6)$$

The first term corresponds to changes in state occupations for fixed state localizations. It represents the NA ET. The second term corresponds to



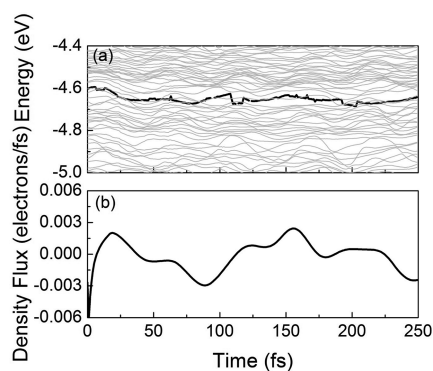


**Figure 4.** (a) Evolution of the energies of the PbSe photoexcited state (thick dark line) and the  $\text{TiO}_2$  conduction band states (thin gray lines). The fluctuation of the photoexcited state energy is small, since it is delocalized over the relatively large and rigid QD. (b) Photoexcited state density flux from QD to  $\text{TiO}_2$ , induced by thermal atomic motions (Figure 2). The flux is computed as the time derivative of the localization of the photoexcited state density on the  $\text{Pb}_{16}\text{Se}_{16}$  cluster. Note that the flux does not represent the photon-induced ET but rather describes the fluctuation of the photoexcited state localization between QD and  $\text{TiO}_2$ .

changes in localizations of the adiabatic states for fixed state occupations. In particular, it describes the adiabatic ET due to a change in the localizations of the adiabatic states from the PbSe QD to the  $\text{TiO}_2$  surface, induced by an atomic motion. The NA and adiabatic contributions to the overall ET are obtained by integrating the first and second term in eq 6 over time. To undergo a transfer, the PE electron in the PbSe QD state has to find a strongly coupled  $\text{TiO}_2$  state via hopping over several uncoupled  $\text{TiO}_2$  CB states. The definition of the NA ET mechanism via the first term of eq 6 includes this effect by considering only those NA transitions that produce the overall shift of the electron density from the QD into  $\text{TiO}_2$ . In particular, if states  $i$  and  $j$  have the same localization, specified by the integral over  $\text{dr}$ , then a NA transition between these states gives zero contribution to ET.

It should be noted that the term “NA ET”, synonymous to “diabatic ET”, is commonly used in the ET literature to describe quantum jumps from the donor to the acceptor state; that is, the jumps occur between diabatic rather than adiabatic states, because the most commonly used ET theory, the Marcus theory, is formulated in the diabatic picture.<sup>99</sup> NA ET is contrasted with adiabatic ET that occurs at a transition state, at which one diabatic curve smoothly transforms into the other diabatic curve, forming a single adiabatic state. If a jump between adiabatic states happens at the transition state, no net ET is created, since the jump counteracts the adiabatic ET. The NA ET mechanism becomes effective away from the transition state, where the adiabatic and diabatic curves coincide. Therefore, one can use both diabatic and adiabatic states in order to represent NA ET and to regard it as a quantum jump from one adiabatic (or diabatic) curve to another.

To simulate the photoinduced ET dynamics, the initial system geometry is selected randomly from the 2 ps adiabatic MD trajectory. Then, the photoexcited state is determined by choosing the lowest energy adiabatic state within the  $\text{TiO}_2$  CB that has high localization on the PbSe QD, as shown in Figure 3a. Often, the photoexcited state is delocalized onto the  $\text{TiO}_2$  surface owing to the strong PbSe– $\text{TiO}_2$  coupling in the present system. The energies and NA couplings between all pairs of states including the photoexcited state and the  $\text{TiO}_2$  states within the relevant energy range are calculated; see Figure 4a. The photoexcited electron density is propagated by solving eq 3 using the second-order differencing scheme and a  $10^{-3}$  fs time step. The electronic propagation time step is 1000 times smaller than the MD time step, since electrons are much lighter than atoms and move faster. The

average behavior of the photoinduced electron injection in the PbSe– $\text{TiO}_2$  system is obtained by sampling several hundred initial conditions from the MD trajectory.

### 3. RESULTS AND DISCUSSION

The time-domain modeling of the PbSe– $\text{TiO}_2$  system provides a detailed picture of the ET dynamics. It can be compared directly with the closely related simulations of ET at the  $\text{TiO}_2$ –chromophore<sup>7,44–49</sup> and  $\text{TiO}_2$ –water<sup>50</sup> interfaces as well as with the electron–phonon relaxation in the PbSe QD.<sup>80,81,85</sup> As discussed below, the PbSe– $\text{TiO}_2$  interface exhibits both similarities and differences with the  $\text{TiO}_2$ –molecule interfaces. The simulations show that the photoinduced electron injection in the PbSe– $\text{TiO}_2$  system successfully competes with the electron–phonon relaxation inside the PbSe QD, in agreement with the experiment.<sup>86,87</sup>

**3.1. Geometric and Electronic Structure of the  $\text{TiO}_2$ –PbSe QD System.** The present work reports the first time-domain atomistic study of the photoinduced electron injection across a  $\text{TiO}_2$ –QD interface. It adopts the simpler of several possible experimental designs, connecting the PbSe nanoparticle directly to  $\text{TiO}_2$ . This setup corresponds to the hydrazine treatment of nanocrystals that produces bare QD surfaces<sup>86</sup> and allows us to focus on the two key components of the interface, PbSe and  $\text{TiO}_2$ , bypassing additional complications due to the presence of QD ligands. The simulation uses the most common (110) surface of rutile, and the smallest PbSe nanocluster that is thermodynamically stable and preserves the topology of bulk PbSe.

Figure 2a shows the geometry of the system relaxed at 0 K. A sample geometry from the MD run at 100 K is presented in Figure 2b. A comparison of these two panels indicates that thermal fluctuations impact the system geometry. The largest scale motion is associated with QD displacement in the plane of the  $\text{TiO}_2$  surface. The top views show that the QD moves both along and perpendicular to the bidentate PbSe– $\text{TiO}_2$  bridge. The side view confirms this observation, indicating further that the PbSe– $\text{TiO}_2$  connection is quite mobile, although chemically stable. In the system geometry optimized at 0 K, the lengths of the two Pb–O bonds are 2.668 and 2.717 Å, while they become 2.630 and 2.729 Å in the sample MD geometry. The corresponding bond angles fluctuate as well, and the top  $\text{TiO}_2$  surface layers move laterally together with the QD. At the same time, the structure of the QD itself changes little. This is in contrast to the alizarin chromophore, which bends considerably because of thermal motions.<sup>45</sup> Inorganic nanocrystals are much more rigid than organic chromophores. As a result, the electron injection dynamics shows notable differences between the two types of systems. One can expect that in the presence of QD ligands the PbSe– $\text{TiO}_2$  system will exhibit additional features associated with more labile molecular chromophores.

Figure 3 shows the electron densities of the donor and acceptor states. The density of the electron donor is delocalized over the whole QD, while the acceptor state is spread nearly uniformly across the  $\text{TiO}_2$  slab. This situation is in contrast to the molecular systems, where the donor states are typically localized over a part of the chromophore, while the acceptor state resembles a surface impurity more than a periodic band.<sup>45–49</sup> The high symmetry and a relatively large size of the QD sensitizer are responsible for the differences. In contrast to the QD, molecular chromophores are composed of many types of atoms and functional groups, which create an asymmetry in the electronic

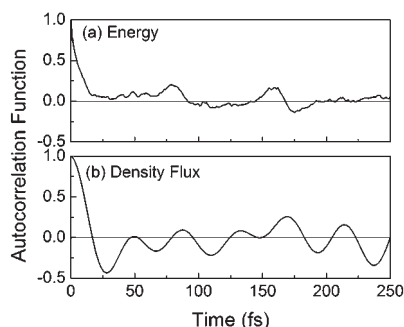


**Figure 5.** Autocorrelation functions (ACFs) of the photoexcited state (a) energy and (b) flux shown in Figure 4. The persistent fluctuation of the density flux ACF is due to the  $800\text{ cm}^{-1}$  polar phonon (Figure 6).

density distribution. Direct coupling of a molecular dye to  $\text{TiO}_2$  produces a strong perturbation in the latter, because dyes contain considerably fewer atoms than QDs, and therefore, they are capable of generating significant local effects. The strong QD– $\text{TiO}_2$  coupling present in the current system in the absence of a bridge results in mixing of the donor and acceptor energy levels shown in Figure 3.

**3.2. Nuclear Dynamics.** The motion of the atoms, exemplified by the two system configurations in Figure 2, affects the energy and density of the photoexcited state (Figure 4). The energy and density fluctuations are significantly smaller in the QD system than with molecular chromophores.<sup>45–49,100</sup> This is because QDs are more rigid than molecules, and QD geometries change much less due to thermal fluctuations and electronic excitation. For instance, the energy of the photoexcited state of the QD fluctuates only by a few tens of millielectronvolts (Figure 4a). In comparison, the corresponding fluctuation is an order of magnitude higher in the alizarin chromophore.<sup>45–48</sup> The localization of the photoexcited state density on the  $\text{Pb}_{16}\text{Se}_{16}$  cluster varies little over time. In order to illustrate this variation more clearly, we depict its time derivative, i.e. flux (Figure 4b).

In addition to creating a canonical ensemble of initial conditions for the photoinduced ET, thermal atomic motions are responsible for both adiabatic and NA ET mechanisms; see eq 6. Atomic motions generate the NA coupling, causing hops between adiabatic states: the NA coupling is directly proportional to the nuclear velocity (eq 4). Atomic motions also shift the adiabatic state densities between the donor and acceptor species, changing state localization and producing adiabatic ET. Even though the fluctuation of the photoexcited state energy is small (Figure 4a), it does produce frequent crossings between the QD and  $\text{TiO}_2$  states. Such crossings of strongly coupled donor and acceptor states can produce transition states for adiabatic ET. The fluctuation of the density of the photoexcited state due to thermal atomic motions is represented in the density flux shown in Figure 4b. The fluctuation is minor and is induced by small-scale atomic motions.

The autocorrelation function (ACF) of the photoexcited state energy is defined as

$$C(t) = \frac{\langle E(t)E(0) \rangle}{\langle E^2 \rangle} \quad (7)$$

It describes how the energy at a particular time depends on its value at earlier times. Generally, poorly correlated random motions give ACFs that decrease rapidly from 1 to 0. Changes

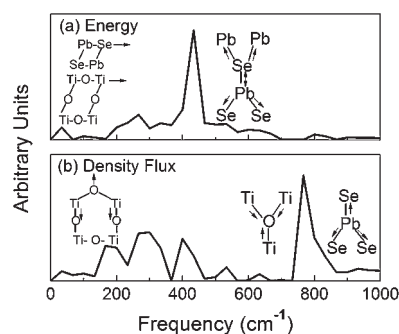


**Figure 6.** Fourier transforms (FTs) of the photoexcited state (a) energy and (b) density flux shown in Figure 4. The drawings schematically illustrate the phonon modes. The dynamics of both energy and density flux are dominated by optical modes. The dominant  $400\text{ cm}^{-1}$  peak seen in part a can be attributed to the second overtone of the longitudinal optical phonon of the  $\text{PbSe}$  QD.<sup>102</sup> The  $800\text{ cm}^{-1}$  peak seen in part b is due to the polaron mode of  $\text{PbSe}$ <sup>103</sup> and high-frequency polar longitudinal optical phonons of  $\text{TiO}_2$ .<sup>104</sup>

that are the result of well-correlated periodic vibrations lead to ACFs that oscillate between 1 and  $-1$ . The ACFs of the photoexcited state energy and flux are shown in Figure 5. Both functions decay rapidly on approximately the same 20 fs time scale. The rapid decay is a result of coupling of the electronic subsystem to multiple phonon modes. The two ACFs show notable qualitative differences at longer times. The energy ACF is quite noisy and exhibits moderate recurrences every 80 fs. The density flux ACF exhibits a much cleaner oscillation with half the period of the energy ACF.

Next, we investigate the phonon modes that couple to the electronic subsystem and promote the ET. In particular, we compute the Fourier transforms (FTs) of the evolving photoexcited state energy and density (Figure 4). The result is shown in Figure 6. The dominant peak at  $400\text{ cm}^{-1}$  seen in the energy FT can be attributed to an overtone of the longitudinal–optical (LO) phonon of the  $\text{PbSe}$  QD.<sup>101</sup> The energy FT also shows a number of moderate size peaks at lower frequencies, arising from a series of transverse-acoustic (TA), transverse-optical (TO), and first- and second-order LO modes.<sup>101</sup> For example, the peak at  $100\text{ cm}^{-1}$  is close to the  $97 \pm 5\text{ cm}^{-1}$  mode of  $\text{PbSe}$ .<sup>86</sup> It is also close to the TO phonon mode at  $104\text{ cm}^{-1}$  of the rutile  $\text{TiO}_2$  (110) surface, arising from the motion of Ti and O atoms in and out of the surface plane.<sup>102</sup> The lowest energy peak seen in the phonon calculated spectra corresponds to the  $\text{PbSe}$  surface optical phonon at the frequency of  $70\text{ cm}^{-1}$  reported in the experiment.<sup>86</sup> The mode is attributed to the electronically coupled two-dimensional QD assemblies. It is less pronounced in our calculation than in the experiment, since the QD replicas present in periodically replicated images of the simulation cell (Figure 2) are separated by vacuum, such that the QDs in the simulated two-dimensional assembly are interacting weakly. The higher frequency signals are overtone combinations of the lower frequency phonons.

The FT of the density flux (Figure 6b) identifies the phonon modes that affect the wave function of the photoexcited state. These modes are somewhat different from the phonons that modulate the state energy, since the energy is computed by averaging over the wave function. The density FT shows a strong peak at  $800\text{ cm}^{-1}$  and a number of weaker signals in the area between 150 and  $400\text{ cm}^{-1}$ . The  $800\text{ cm}^{-1}$  vibration is associated

with the polaron mode of PbSe,<sup>103</sup> as well as with the high-frequency polar longitudinal optical phonons of TiO<sub>2</sub> that play a dominant role in the TiO<sub>2</sub> polaron formation.<sup>104</sup> These atomic motions polarize the PbSe–TiO<sub>2</sub> system and, therefore, couple electrostatically to the excited electron density. The polar vibrations at 800 cm<sup>−1</sup> should be regarded as very high frequency modes, considering the large atomic weights of the elements forming the PbSe–TiO<sub>2</sub> interface. Because these modes involve local displacements of atoms with respect to each other, they have little influence on the excited state energy (Figure 6a), which is computed by averaging over the state density and, therefore, averages out local motions. The signals between 150 and 400 cm<sup>−1</sup> arise from overtones of acoustic and optical modes, as discussed in the previous paragraph.

It may appear surprising that the ultrafast, 10 fs ET process is promoted by vibrational motions with frequencies of 800 cm<sup>−1</sup> or less (Figure 6), since the period of the 800 cm<sup>−1</sup> frequency mode is about 40 fs. The 10 fs ET requires only a quarter of this period. The ultrafast ET becomes possible due to a high density of acceptor states. Then, a fraction of the vibrational period leads to a crossing of the donor and acceptor states (see Figure 4a), resulting in adiabatic ET. A similar observation was made in our earlier studies of the alizarin–TiO<sub>2</sub> system, in which the 6 fs ET was driven by modes with frequencies of 1000 cm<sup>−1</sup> or less.<sup>47</sup> Further evidence supporting multiple acceptor states was provided by our study of the temperature dependence of the adiabatic ET in the alizarin–TiO<sub>2</sub> system.<sup>46</sup> The Arrhenius expression  $k_{ad} = \kappa \nu \exp(\Delta G/kT)$  for the temperature dependence of the ET rate contains the nonadiabaticity,  $\kappa$ , and frequency,  $\nu$ , prefactors. The nonadiabaticity parameter  $\kappa$  is close to one in systems with dominantly adiabatic ET. The study<sup>46</sup> showed that the frequency prefactor was larger than the vibrational frequencies available in the alizarin–TiO<sub>2</sub> system, excluding hydrogen vibrations that had little contribution to the ET process. This observation indicated that multiple acceptor states were involved simultaneously during ET.

It is instructive to consider the similarities and differences in the phonon modes that couple to the photoexcited electron at the QD–TiO<sub>2</sub> interface studied here and the molecule–TiO<sub>2</sub> interfaces investigated earlier.<sup>7,44–50,100</sup> In both cases, the electron–phonon coupling arises as a result of vibrations with frequencies below 1000 cm<sup>−1</sup>. However, in the present case, the active modes represent the high-energy end of the phonon spectrum, since the QD chromophore is composed of heavy elements. In molecular chromophores, the modes below 1000 cm<sup>−1</sup> correspond to low frequency bending and torsional motions. The high-frequency molecular vibrations reside above 1000 cm<sup>−1</sup>, and even beyond 3000 cm<sup>−1</sup>. This is because organic molecules are composed primarily of light elements from the first and second rows of the Periodic Table. The phonon spectra in Figure 6 of the current work are shifted toward the highest frequency optical modes available in the PbSe–TiO<sub>2</sub> system, while the highest peaks in the vibrational spectra in Figure 7a of ref 47 reside in the low-frequency mode region of the organic chromophore. Vibrational wave packet motion due to high frequency chromophore modes with time scales similar to or shorter than the ET time can also contribute to the electron injection process,<sup>105</sup> as detected in time-resolved laser experiments.<sup>106</sup>

The difference in the types of modes driving the photoexcited electron dynamics in the systems involving a semiconductor QD and an organic molecule likely arises due to a small variation between the acoustic and optical mode frequencies for the QD,

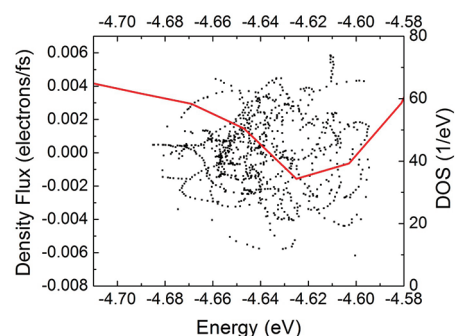


**Figure 7.** TiO<sub>2</sub> DOS within the simulation cell (red line) and the photoexcited state density flux between the QD and TiO<sub>2</sub> (black squares) as functions of energy. Computed as the time derivative of the localization of the photoexcited state density on the QD, the flux describes the fluctuation of the state localization between QD and TiO<sub>2</sub>. The dip in the DOS correlates with a larger density fluctuation. Higher TiO<sub>2</sub> DOS tends to average out fluctuations in the photoexcited state localization.

compared to the molecule. *A priori*, one may expect optical modes to provide stronger electron–phonon coupling, since the coupling, eq 4, depends on mode velocity, and at a given temperature, the velocity is larger for higher frequency vibrations. This argument works for QD, since both optical and acoustic modes are activated at the experimental temperature range. In contrast, high-frequency vibrations of molecular chromophores reside at energies that are an order of magnitude higher than  $k_B T$  and remain essentially inactive at ambient and low temperatures. High-frequency vibrations can have a substantial influence on the ET process,<sup>105,106</sup> even at zero temperature, if a shift in the equilibrium geometries of the ground and excited chromophore states, combined with a strong electron–phonon coupling, is capable of producing a vibronic progression of Franck–Condon factors along the high-frequency mode coordinate.<sup>42</sup>

The behavior of the wet-electron system<sup>51</sup> resembles that of the chromophore–TiO<sub>2</sub> interface rather than the QD–TiO<sub>2</sub> interface. Primarily low frequency bending and librational modes of water are involved in the ET dynamics at the wet TiO<sub>2</sub> surface.<sup>50</sup>

Figure 7 shows the distribution of the photoexcited state energy and its density flux. The width of the photoexcited state energy distribution agrees with the 10 fs electron injection time: the lifetime-width product is on the order of Planck's constant. The figure also presents the TiO<sub>2</sub> density of states (DOS) within the energy region that contains the QD photoexcited state. The photoexcited state density flux is computed as the time-derivative of the localization of the photoexcited state density on the QD. It describes the fluctuation of the state localization between QD and TiO<sub>2</sub>. There exists no correlation between the state energy and its localization; however, the fluctuation in the state localization increases when the DOS dips. Normally, electronic DOS grows with energy, but the photoexcited state is already in the region of high TiO<sub>2</sub> DOS. The local dip in the DOS is related to the  $t_{2g}$ – $e_g$  splitting of the Ti 3d orbitals that form the TiO<sub>2</sub> CB.<sup>107</sup> The increased fluctuation in the photoexcited state localization on PbSe associated with the DOS minimum can be rationalized by a less even coupling between PbSe and TiO<sub>2</sub>. In the region of decreased DOS, the QD interacts with fewer TiO<sub>2</sub> states, and therefore, the interface properties become less averaged. Higher TiO<sub>2</sub> DOS tends to average out the properties of the interface and, in particular, the fluctuations in the



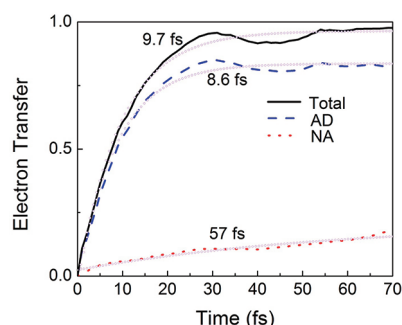


**Figure 8.** Average electron transfer (ET) dynamics. The solid black, dashed blue, and dotted red lines represent the total, adiabatic (AD), and nonadiabatic (NA) ET, respectively. The open circles are fits (eq 8) with the time scales shown in the figure. The AD ET is faster than the NA ET and provides the dominant ET mechanism in the current system.

photoexcited state localization. The differences between the average behavior and individual members of the canonical ensemble of QD–TiO<sub>2</sub> systems are emphasized further in the following section, which described the ET dynamics.

**3.3. Electron Transfer Dynamics.** The time-domain *ab initio* simulation shows that the photoinduced ET from the Pb<sub>16</sub>Se<sub>16</sub> QD into the TiO<sub>2</sub> surface occurs on a 10 fs time scale (Figure 8), which is on the same order of magnitude as the sub-50-fs experimental injection time.<sup>86,87</sup> As should be expected, the simulated dynamics are faster than those of the measured ET, because the QD used in the calculation is smaller than that in the experiment. The reduced system size implies that the QD–TiO<sub>2</sub> coupling is stronger and that the photoexcited state is located closer to TiO<sub>2</sub>. The vibrational motions driving the ET process have higher frequencies in smaller QDs, additionally accelerating the ET dynamics. Further, the simulation assumed that the QD interacts with the substrate directly, bypassing a possible bridge. The hydrazine treatment of the nanocrystals was aimed to create this situation in the experiment;<sup>86</sup> however, it is possible that some ligands remained on the QD surface, reducing the QD–TiO<sub>2</sub> coupling. Given these considerations, the agreement between theory and experiment is very good.

The strong coupling between the PbSe QD and the TiO<sub>2</sub> surface, together with the high density of TiO<sub>2</sub> states at the photoexcited state energy, are beneficial for the ultrafast ET. The strong coupling drives adiabatic ET, while the high density of acceptor states favors NA ET. The calculations indicate that the photoinduced electron injection occurs primarily by the adiabatic mechanism, which is responsible for about 80% of the overall ET. The NA mechanism generates the remaining 20%. The two mechanisms compete with each other. Adiabatic ET requires a crossing of the donor and acceptor states, driven by an atomic motion along the reaction coordinate. It involves a change of localization of the occupied adiabatic state from the donor to the acceptor. NA ET proceeds by a quantum transition between different adiabatic states localized on QD and TiO<sub>2</sub>. While NA ET does not require a state crossing, it does involve a tunneling barrier and an energy gap, which become smaller around a crossing region.

The time scales of the total, adiabatic, and NA ET were determined by fitting the calculated data with the exponential function

$$y = y_0 + A \exp(-x/t) \quad (8)$$

where  $t$  is the ET time scale. The  $A$  constant reflects the amplitudes of the adiabatic and NA contributions to the overall ET. The small  $y_0$

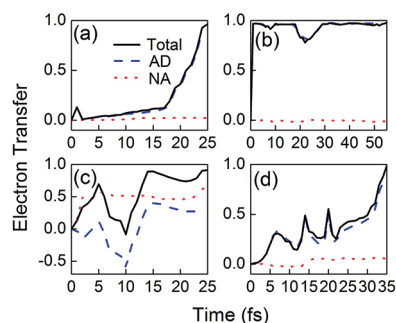


**Figure 9.** Examples of individual ET events. The lines have the same meaning as in Figure 8. (a) A relatively long “waiting” time is required prior to ET that occurs by the AD mechanism. (b) A rapid AD ET. (c) A sequence of forward NA ET, backward AD ET, and forward AD ET. (d) A gradual AD ET accompanied by fluctuations in the ET progress and a small NA component.

term is needed to reflect the fact that the ET is not exponential but rather Gaussian at the early time. The fits show that the adiabatic ET proceeds 10% faster than the overall ET, while the NA component is 10 times slower.

The ET dynamics averaged over all NAMD runs present a straightforward description of the system behavior. A more detailed picture is provided by examples of individual ET events (Figure 9). These examples illustrate interesting interplay between adiabatic and NA ET mechanisms, and they exhibit a broad range of possibilities for the ET dynamics. The variety of ET scenarios is completely hidden in the average description. Thus, Figure 9a shows an example that involves a “waiting” period required for the photoexcited electron to find an adiabatic transfer channel. Figure 9b illustrates an almost instantaneous adiabatic ET. The example of Figure 9c exhibits a very complex behavior. Initially, the electron is injected by the NA mechanism outside a donor–acceptor state crossing. However, 5 fs later, such crossing is encountered, but instead of forward transfer, the electron returns to the QD adiabatically. In another 5 fs, the electron again moves onto TiO<sub>2</sub>, this time adiabatically, as a result of the same state crossing that enabled the back-transfer. The oscillation in the ET progress is driven by atomic motions that produce recrossings of the adiabatic ET barrier. Finally, Figure 9d shows gradual ET with fluctuations. Here, the primarily adiabatic ET is accompanied by a small NA component. Each donor–acceptor adiabatic state crossing generates a forward or a backward ET. The overall progress toward forward ET is determined entropically by the fact that there are many more TiO<sub>2</sub> than PbSe states within the relevant energy window. The individual ET events shown in Figure 9 represent examples of electron injection that can be detected by single-molecule spectroscopies in the future. Despite the diversity in the ET dynamics, the average ET is quite straightforward in the current system. The photoexcited electron injection from the PbSe QD into the TiO<sub>2</sub> surface is very fast and proceeds primarily by the adiabatic mechanism, as shown in Figure 8.

Finally, it is valuable to compare the ET dynamics in the QD–TiO<sub>2</sub> system to those at the molecule–TiO<sub>2</sub> and solvent–TiO<sub>2</sub> interfaces, represented by the alizarin–TiO<sub>2</sub> system<sup>45–48</sup> and the wet-electron.<sup>50</sup> In all three cases, the electron donor is attached directly to the TiO<sub>2</sub> surface without any bridge. Therefore, the donor–acceptor coupling is strong, and the photoinduced electron injection is ultrafast. The main differences stem from the size and

dimensionality of the donor species. Both the QD and the molecule are localized species; however, the QD is notably larger than the molecule. In contrast, the water layer in the wet-electron system is a delocalized two-dimensional object. The ET rate correlates with the distance from the electron donor to the TiO<sub>2</sub> acceptor. In particular, the rate decreases in the sequence ranging from water, to the molecule, to the QD, as the center-of-mass of the donor state moves farther away from the surface. The ET mechanism depends on the dimensionality of the donor. The injection from the localized donor states of the QD and the molecule is dominantly adiabatic. In contrast, the injection from the two-dimensional water layer in the wet-electron system exhibits a high, 50% NA component, which is unexpected, since the donor–acceptor coupling is strong in this case as well. The NA mechanism is efficient for the wet-electron because it is delocalized over two dimensions and is able to couple with a dense manifold of delocalized TiO<sub>2</sub> CB states. The high density of acceptor states in this case favors the NA mechanism, which can be described, for instance, by Fermi's golden rule.<sup>68</sup> According to Fermi's golden rule, the NA rate is directly proportional to the acceptor DOS. In comparison to the wet-electron, the QD and molecular donor states interact only with TiO<sub>2</sub> surface states localized in the nearby spatial region. The DOS of such states is significantly lower than the TiO<sub>2</sub> CB DOS. All three systems exhibit diverse scenarios for individual electron injection events, involving a complex interplay of ET mechanisms, time scales, and phonon dynamics.

#### 4. CONCLUSIONS

Motivated by the recent experimental work aimed at development of efficient photovoltaic devices, we simulated the photoinduced ET in the nanoscale system composed of a PbSe QD adsorbed on a TiO<sub>2</sub> surface. The use of QDs as TiO<sub>2</sub> sensitizers carries the potential of increasing solar cell voltage by rapid extraction of hot electrons<sup>86</sup> and enhancing current via generation of multiple charge carriers per absorbed photons.<sup>28</sup> The simulation was performed in real time and at the atomistic level, using the state-of-the-art approach combining TDDFT with NAMD.<sup>42,79–81</sup> Showing good agreement with the experiment,<sup>86,87</sup> the reported study directly mimics the observed time-resolved ET process, establishes the mechanisms responsible for the movement of charge through the system, identifies the vibrational motions that promote the transfer, and provides a detailed understanding of the ET dynamics. The work connects directly with the earlier simulations of the ET processes at the TiO<sub>2</sub>–molecule<sup>7,44–49</sup> and TiO<sub>2</sub>–water<sup>50</sup> interfaces, and in semiconductor QDs.<sup>80,81,85</sup>

The simulation supports the experimental observation that the photoinduced electron injection in the PbSe–TiO<sub>2</sub> system can successfully compete with the electron–phonon relaxation inside the PbSe QD. The ultrafast ET proceeds primarily by the adiabatic mechanism, due to strong coupling between the donor and acceptor subsystems. The weak NA transfer component is nearly an order of magnitude slower than the adiabatic ET. Adiabatic transfer results from a vibrational motion driving the electronic subsystem over a transition state. NA ET occurs by a quantum transition between electron donor and acceptor states. The complex interplay of the ET mechanisms, donor–acceptor and electron–phonon interactions, and phonon dynamics creates a broad spectrum of electron injection scenarios, including nearly instantaneous adiabatic injection; gradual, stepwise adiabatic ET; and combinations of forward transfer and back-transfer by both NA and adiabatic mechanisms. The highest frequency

vibrations available in the PbSe–TiO<sub>2</sub> system, in particular polar Pb–Se and Ti–O stretches, promote the ET. These polar modes are able to shift the electronic density between the donor and acceptor species and to facilitate the adiabatic ET. Lower frequency modes, including TiO<sub>2</sub> and PbSe surface vibrations, create an inhomogeneous distribution of initial conditions for the photoinduced transfer.

The QD–TiO<sub>2</sub> interface exhibits both similarities and differences with the TiO<sub>2</sub>–molecule interfaces. The similarities arise due to strong electronic donor–acceptor coupling in these systems, in the absence of a bridge. The strong coupling induces efficient and ultrafast photoinduced electron injection by the adiabatic mechanism. A diverse set of states present in the system simultaneously, ranging from quasi-zero-dimensional QD and molecular states, to two-dimensional surface states, to three-dimensional states of bulk TiO<sub>2</sub>, generates a variety of complex individual ET events. The differences in the electron injection that takes place from molecular and QD sensitizers can be attributed to the larger size and higher rigidity of inorganic nanocrystals compared to molecules. Strong electronic donor–acceptor interaction localizes the states in molecular systems: the donor typically involves only part of the chromophore, and the acceptor resembles a surface impurity. In contrast, in the current QD–TiO<sub>2</sub> system, the electron donor density is spread over the whole QD, while the acceptor density is distributed nearly uniformly across the TiO<sub>2</sub> slab. This remains true in spite of the small QD used in the present study: its size is comparable to that of molecular chromophores. High-frequency optical modes are much more active in the QD case than with molecular sensitizers. One may expect high-frequency oscillations to be active in all systems; however, in general, they remain dormant in molecules, since their energy is significantly higher than thermal energy under ambient conditions. In contrast, thermal and optical mode energies are of the same order of magnitude in QDs, since QDs are composed of heavy elements. The wet-electron presents an interesting example of a molecular system supporting a delocalized electron donor state. As a result, and in spite of the strong donor–acceptor coupling, the NA mechanism contributes significantly to the ET process, because the two-dimensional donor state of the wet-electron couples with a dense manifold of delocalized TiO<sub>2</sub> CB states. In the presence of QD ligands, the photon-induced ET at the QD–TiO<sub>2</sub> interface should exhibit features associated with more labile molecular chromophores. The simulation of the excited state dynamics in the QD–TiO<sub>2</sub> system provides valuable insights into the interfacial ET processes involved in a wide variety of applications, including photovoltaics, solar hydrogen production, molecular electronics and spintronics, catalysis, and electrolysis.

#### ■ ASSOCIATED CONTENT

**S Supporting Information.** Structure of the simulated system optimized at  $T = 0$  K, and the dimensions of the simulation cell, along with the XYZ coordinates of this structure; see the left panel of Figure 2 of the main text. This material is available free of charge via the Internet at <http://pubs.acs.org>.

#### ■ AUTHOR INFORMATION

##### Corresponding Author

[oleg.prezhdo@rochester.edu](mailto:oleg.prezhdo@rochester.edu)



## ■ ACKNOWLEDGMENT

The authors are grateful to Amanda Neukirch for comments on the manuscript. R.L. thanks the IRCSET-Marie Curie International Mobility Fellowship in Science, Engineering and Technology (reference no. PD/2010/INSP/1485). O.P. acknowledges the NSF Grant CHE-1050405 dedicated to the method development and the DOE Grant DE-FG02-05ER15755 supporting the quantum dot studies.

## ■ REFERENCES

- (1) Brown, G. E.; Henrich, V. E.; Casey, W. H.; Clark, D. L.; Eggleston, C.; Felmy, A.; Goodman, D. W.; Grätzel, M.; Maciel, G.; McCarthy, M. I.; Neelson, K. H.; Sverjensky, D. A.; Toney, M. F.; Zachara, J. M. *Chem. Rev.* **1998**, *99*, 77.
- (2) Nitzan, A.; Ratner, M. A. *Science* **2003**, *300*, 1384.
- (3) Fan, F.-R. F.; Yao, Y.; Cai, L.; Cheng, L.; Tour, J. M.; Bard, A. J. *J. Am. Chem. Soc.* **2004**, *126*, 4035.
- (4) Hagfeldt, A.; Grätzel, M. *Acc. Chem. Res.* **2000**, *33*, 269.
- (5) Anderson, N. A.; Lian, T. *Annu. Rev. Phys. Chem.* **2005**, *56*, 491.
- (6) Kamat, P. V. *J. Phys. Chem. C* **2007**, *111*, 2834.
- (7) Duncan, W. R.; Prezhdo, O. V. *Annu. Rev. Phys. Chem.* **2007**, *58*, 143.
- (8) Prezhdo, O. V.; Duncan, W. R.; Prezhdo, V. V. *Acc. Chem. Res.* **2008**, *41*, 339.
- (9) Tang, J. W.; Durrant, J. R.; Klug, D. R. *J. Am. Chem. Soc.* **2008**, *130*, 13885.
- (10) Roy, P.; Das, C.; Lee, K.; Hahn, R.; Ruff, T.; Moll, M.; Schmuki, P. *J. Am. Chem. Soc.* **2011**, *133*, 5629.
- (11) Jiang, D.; Zhao, H.; Zhang, S.; John, R. J. *Catal.* **2004**, *223*, 212.
- (12) Zhao, W.; Ma, W.; Chen, C.; Zhao, J.; Shuai, Z. *J. Am. Chem. Soc.* **2004**, *126*, 4782.
- (13) Anfuso, C. L.; Snoberger, R. C.; Ricks, A. M.; Liu, W. M.; Xiao, D. Q.; Batista, V. S.; Lian, T. Q. *J. Am. Chem. Soc.* **2011**, *133*, 6922.
- (14) Kamat, P. V. *Chem. Rev.* **1993**, *93*, 267.
- (15) Zhu, X. Y. *Annu. Rev. Phys. Chem.* **1994**, *45*, 113.
- (16) Yang, C.-C.; Yu, Y.-H.; van der Linden, B.; Wu, J. C. S.; Mul, G. *J. Am. Chem. Soc.* **2010**, *132*, 8398.
- (17) Guo, Z. Y.; Jenekhe, S. A.; Prezhdo, O. V. *Phys. Chem. Chem. Phys.* **2011**, *13*, 7630.
- (18) Zimmerman, P. M.; Zhang, Z. Y.; Musgrave, C. B. *Nature Chem.* **2010**, *2*, 648.
- (19) Wang, C. L.; Wang, F. H.; Yang, X. D.; Li, Q. K.; Shuai, Z. G. *Org. Electron.* **2008**, *9*, 635.
- (20) Park, S. I.; et al. *Science* **2009**, *325*, 977.
- (21) Jin, S. Y.; Song, N. H.; Lian, T. Q. *ACS Nano* **2010**, *4*, 1545.
- (22) Fang, Z.; Eshbaugh, A. A.; Schanze, K. S. *J. Am. Chem. Soc.* **2011**, *133*, 3063.
- (23) Kennedy, R. D.; Ayzner, A. L.; Wanger, D. D.; Day, C. T.; Halim, M.; Khan, S. I.; Tolbert, S. H.; Schwartz, B. J.; Rubin, Y. *J. Am. Chem. Soc.* **2008**, *130*, 17290.
- (24) Kohler, A.; dos Santos, D. A.; Beljonne, D.; Shuai, Z.; Bredas, J. L.; Holmes, A. B.; Kraus, A.; Mullen, K.; Friend, R. H. *Nature* **1998**, *392*, 903.
- (25) Tung, V. C. T. V. C.; Huang, J. H.; Tevis, I.; Kim, F.; Kim, J.; Chu, C. W.; Stupp, S. I.; Huang, J. X. *J. Am. Chem. Soc.* **2011**, *133*, 4940.
- (26) Tributsch, H. *Coord. Chem. Rev.* **2004**, *248*, 1511.
- (27) Nozik, A. J. *Phys. E (Amsterdam, Neth.)* **2002**, *14*, 115.
- (28) Sambur, J. B.; Novet, T.; Parkinson, B. A. *Science* **2010**, *330*, 63.
- (29) O'Regan, B.; Grätzel, M. *Nature* **1991**, *353*, 737.
- (30) Nishimura, S.; Abrams, N.; Lewis, B. A.; Halaoui, L. I.; Mallouk, T. E.; Benkstein, K. D.; van de Lagemaat, J.; Frank, A. J. *J. Am. Chem. Soc.* **2003**, *125*, 6306.
- (31) Redfern, P. C.; Zapol, P.; Curtiss, L. A.; Rajh, T.; Thurnauer, M. C. *J. Phys. Chem. B* **2003**, *107*, 11419.
- (32) Xiao, D. Q.; Martini, L. A.; Snoberger, R. C.; Crabtree, R. H.; Batista, V. S. *J. Am. Chem. Soc.* **2011**, *133*, 9014.
- (33) Terranova, U.; Bowler, D. R. *J. Phys. Chem. C* **2010**, *114*, 6491.
- (34) Standridge, S. D.; Schatz, G. C.; Hupp, J. T. *J. Am. Chem. Soc.* **2009**, *131*, 8407.
- (35) Persson, P.; Bergström, R.; Lunell, S. *J. Phys. Chem. B* **2000**, *104*, 10348.
- (36) Pal, S. K.; Sundstrom, V.; Galoppini, E.; Persson, P. *Dalton Trans.* **2009**, 10021.
- (37) Martsinovich, N.; Troisi, A. *J. Phys. Chem. C* **2011**, *115*, 11781.
- (38) Ramakrishna, S.; Seideman, T.; Willig, F.; May, V. *J. Chem. Sci.* **2009**, *121*, 589.
- (39) Rego, L. G. C.; Batista, V. S. *J. Am. Chem. Soc.* **2003**, *125*, 7989.
- (40) Abuabara, S. G.; Rego, L. G. C.; Batista, V. S. *J. Am. Chem. Soc.* **2005**, *127*, 18234.
- (41) Ramakrishna, S.; Willig, F.; May, V.; Knorr, A. *J. Phys. Chem. B* **2003**, *107*, 607.
- (42) Li, J. R.; Kondov, I.; Wang, H. B.; Thoss, M. *J. Phys. Chem. C* **2010**, *114*, 18481.
- (43) Thoss, M.; Kondov, I.; Wang, H. *Chem. Phys.* **2004**, *304*, 169.
- (44) Duncan, W. R.; Craig, C. F.; Prezhdo, O. V. *J. Am. Chem. Soc.* **2007**, *129*, 8528.
- (45) Duncan, W. R.; Prezhdo, O. V. *J. Phys. Chem. B* **2005**, *109*, 17998.
- (46) Duncan, W. R.; Prezhdo, O. V. *J. Am. Chem. Soc.* **2008**, *130*, 9756.
- (47) Duncan, W. R.; Stier, W. M.; Prezhdo, O. V. *J. Am. Chem. Soc.* **2005**, *127*, 7941.
- (48) Stier, W.; Duncan, W. R.; Prezhdo, O. V. *Adv. Mater.* **2004**, *16*, 240.
- (49) Stier, W.; Prezhdo, O. V. *J. Phys. Chem. B* **2002**, *106*, 8047.
- (50) Fischer, S. A.; Duncan, W. R.; Prezhdo, O. V. *J. Am. Chem. Soc.* **2009**, *131*, 15483.
- (51) Onda, K.; Li, B.; Zhao, J.; Jordan, K. D.; Yang, J. L.; Petek, H. *Science* **2005**, *308*, 1154.
- (52) Mora-Sero, I.; Giménez, S.; Fabregat-Santiago, F.; Gómez, R.; Shen, Q.; Toyoda, T.; Bisquert, J. *Acc. Chem. Res.* **2009**, *42*, 1848.
- (53) Prezhdo, O. V. *Chem. Phys. Lett.* **2008**, *460*, 1.
- (54) Prezhdo, O. V. *Acc. Chem. Res.* **2009**, *42*, 2005.
- (55) Robel, I.; Subramanian, V.; Kuno, M.; Kamat, P. V. *J. Am. Chem. Soc.* **2006**, *128*, 2385.
- (56) Schaller, R. D.; Klimov, V. I. *Phys. Rev. Lett.* **2004**, *92*, 186601.
- (57) Ellingson, R. J.; Beard, M. C.; Johnson, J. C.; Yu, P.; Micic, O. I.; Nozik, A. J.; Shabaev, A.; Efros, A. L. *Nano Lett.* **2005**, *5*, 865.
- (58) Schaller, R. D.; Pietryga, J. M.; Goupalov, S. V.; Petruska, M. A.; Ivanov, S. A.; Klimov, V. I. *Phys. Rev. Lett.* **2005**, *95*, 086801.
- (59) Nozik, A. J.; Beard, M. C.; Luther, J. M.; Law, M.; Ellingson, R. J.; Johnson, J. C. *Chem. Rev.* **2010**, *110*, 6873.
- (60) Beard, M. C.; Midgett, A. G.; Hanna, M. C.; Luther, J. M.; Hughes, B. K.; Nozik, A. J. *Nano Lett.* **2010**, *10*, 3019.
- (61) McGuire, J. A.; Joo, J.; Pietryga, J. M.; Schaller, R. D.; Klimov, V. I. *Acc. Chem. Res.* **2008**, *41*, 1810.
- (62) Nair, G.; Chang, L. Y.; Geyer, S. M.; Bawendi, M. G. *Nano Lett.* **2011**, *11*, 2145.
- (63) Pijpers, J. J. H.; Ulbricht, R.; Tielrooij, K. J.; Osherov, A.; Golan, Y.; Delerue, C.; Allan, G.; Bonn, M. *Nat. Phys.* **2009**, *5*, 811.
- (64) Pandey, A.; Guyot-Sionnest, P. *Science* **2008**, *322*, 929.
- (65) Efros, A. L.; Rosen, M. *Annu. Rev. Mater. Sci.* **2000**, *30*, 475.
- (66) Califano, M.; Franceschetti, A.; Zunger, A. *Nano Lett.* **2005**, *5*, 2360.
- (67) Califano, M.; Zunger, A.; Franceschetti, A. *Nano Lett.* **2004**, *4*, 525.
- (68) Rabani, E.; Baer, R. *Nano Lett.* **2008**, *8*, 4488.
- (69) Rabani, E.; Baer, R. *Chem. Phys. Lett.* **2010**, *496*, 227.
- (70) Kilina, S.; Ivanov, S.; Tretiak, S. *J. Am. Chem. Soc.* **2009**, *131*, 7717.
- (71) Shockley, W.; Queisser, H. J. *Detailed Balance Limit of Efficiency of p-n Junction Solar Cells*; AIP: 1961; Vol. 32.
- (72) Fischer, S. A.; Prezhdo, O. V. *J. Phys. Chem. C* **2011**, *115*, 10006.

- (73) Fischer, S. A.; Madrid, A. B.; Isborn, C. M.; Prezhdo, O. V. *J. Phys. Chem. Lett.* **2009**, *1*, 232.
- (74) Fischer, S. A.; Isborn, C. M.; Prezhdo, O. V. *Chem. Sci.* **2011**, *2*, 400.
- (75) Isborn, C. M.; Kilina, S. V.; Li, X. S.; Prezhdo, O. V. *J. Phys. Chem. C* **2008**, *112*, 18291.
- (76) Isborn, C. M.; Prezhdo, O. V. *J. Phys. Chem. C* **2009**, *113*, 12617.
- (77) Madrid, A. B.; Hyeon-Deuk, K.; Habenicht, B. F.; Prezhdo, O. V. *ACS Nano* **2009**, *3*, 2487.
- (78) Kamisaka, H.; Kilina, S. V.; Yamashita, K.; Prezhdo, O. V. *J. Phys. Chem. C* **2008**, *112*, 7800.
- (79) Kamisaka, H.; Kilina, S. V.; Yamashita, K.; Prezhdo, O. V. *Nano Lett.* **2006**, *6*, 2295.
- (80) Kilina, S. V.; Craig, C. F.; Kilin, D. S.; Prezhdo, O. V. *J. Phys. Chem. C* **2007**, *111*, 4871.
- (81) Kilina, S. V.; Kilin, D. S.; Prezhdo, O. V. *ACS Nano* **2009**, *3*, 93.
- (82) Hyeon-Deuk, K.; Madrid, A. B.; Prezhdo, O. V. *Dalton Trans.* **2009**, 10069.
- (83) Hyeon-Deuk, K.; Prezhdo, O. V. *Nano Lett.* **2011**, *11*, 1845.
- (84) Chen, L. L.; Bao, H.; Tan, T. Z.; Prezhdo, O. V.; Ruan, X. L. *J. Phys. Chem. C* **2011**, *115*, 11400.
- (85) Bao, H.; Habenicht, B. F.; Prezhdo, O. V.; Ruan, X. L. *Phys. Rev. B* **2009**, *79*, 235306.
- (86) Tisdale, W. A.; Williams, K. J.; Timp, B. A.; Norris, D. J.; Aydil, E. S.; Zhu, X.-Y. *Science* **2010**, *328*, 1543.
- (87) Tisdale, W. A.; Zhu, X. Y. *Proc. Natl. Acad. Sci. U.S.A.* **2011**, *108*, 965.
- (88) Craig, C. F.; Duncan, W. R.; Prezhdo, O. V. *Phys. Rev. Lett.* **2005**, *95*, 163001.
- (89) Fischer, S. A.; Habenicht, B. F.; Madrid, A. B.; Duncan, W. R.; Prezhdo, O. V. *J. Chem. Phys.* **2011**, *134*, 024102.
- (90) Habenicht, B. F.; Prezhdo, O. V. *Phys. Rev. Lett.* **2008**, *100*, 197402.
- (91) Habenicht, B. F.; H. B. F.; Prezhdo, O. V. *J. Phys. Chem. C* **2009**, *113*, 14067.
- (92) Habenicht, B. F.; Craig, C. F.; Prezhdo, O. V. *Phys. Rev. Lett.* **2006**, *96*, 166803.
- (93) Cramer, C. J.; Truhlar, D. G. *Phys. Chem. Chem. Phys.* **2009**, *11*, 10757.
- (94) Kresse, G.; Furthmüller, J. *Phys. Rev. B* **1996**, *54*, 11169.
- (95) Perdew, J. P.; Burke, K.; Ernzerhof, M. *Phys. Rev. Lett.* **1996**, *77*, 3865.
- (96) Blochl, P. E. *Phys. Rev. B* **1994**, *50*, 17953.
- (97) Jasper, A. W.; Nangia, S.; Zhu, C. Y.; Truhlar, D. G. *Acc. Chem. Res.* **2006**, *39*, 101.
- (98) Prezhdo, O. V.; Duncan, W. R.; Prezhdo, V. V. *Prog. Surf. Sci.* **2009**, *84*, 30.
- (99) Newton, M. D.; Sutin, N. *Annu. Rev. Phys. Chem.* **1984**, *35*, 437.
- (100) Stier, W.; Prezhdo, O. V. *Isr. J. Chem.* **2002**, *42*, 213.
- (101) Kigel, A.; Brumer, M.; Maikov, G. I.; Sashchiuk, A.; Lifshitz, E. *Small* **2009**, *5*, 1675.
- (102) Lindsay, R.; Wander, A.; Ernst, A.; Montanari, B.; Thornton, G.; Harrison, N. M. *Phys. Rev. Lett.* **2005**, *94*, 246102.
- (103) Yang, A. L. W.; H., Z.; Li, Z. F.; Qiu, D. J.; Chang, Y.; Li, J. F.; McCann, P. J.; Fang, X. M. *Chin. Phys. Lett.* **2000**, *17*, 3.
- (104) Baumard, J.-F.; Gervais, F. *Phys. Rev. B* **1977**, *15*, 2316.
- (105) Kondov, I.; Thoss, M.; Wang, H. B. *J. Phys. Chem. A* **2006**, *110*, 1364.
- (106) Zimmermann, C.; Willig, F.; Ramakrishna, S.; Burfeindt, B.; Pettinger, B.; Eichberger, R.; Storck, W. *J. Phys. Chem. B* **2001**, *105*, 9245.
- (107) See, A. K.; Thayer, M.; Bartynski, R. A. *Phys. Rev. B* **1993**, *47*, 13722.